Thermoelectric properties of Mg 2 X (X 5 Si, Ge) based bulk and quantum well systems

1 author:

Övgü Ceyda Yelgel

Recep Tayyip Erdoğan Üniversitesi

14 PUBLICATIONS   **150** CITATIONS

SEE PROFILE

Some of the authors of this publication are also working on these related projects:

Project   Theoretical Investigation of Thermoelectric Properties of Mg2X (X=Si, Ge, Sn) Based Thermoelectrics View project

Thermoelectric properties of Mg₂X (X = Si, Ge) based bulk and quantum well systems

Övgü Ceyda Yelgel

Faculty of Engineering, Department of Materials Science and Nanotechnology Engineering, Recep Tayyip Erdoğan University, 53100 Rize, Turkey

Mg₂X (X = Si, Ge) compounds are promising thermoelectric materials for middle temperature applications due to good thermoelectric properties, nontoxicity, and abundantly available constituent elements. So far, these materials used in applications have all been in bulk form. Herein we report a full theory of thermoelectric transport properties of 3D bulk and 2D quantum well systems. The main aim of this present work is to show the effect of quantum confinement on the enhancement of the thermoelectric figure of merit theoretically. Results are given for n-type Mg₂Si$_{0.5}$Ge$_{0.5}$ solid solutions and n-type Mg₂Si/Mg₂Ge/Mg₂Si quantum well systems where the values of well widths are taken as 10 nm, 15 nm, and 20 nm, respectively. The n-type doping is made by using Sb- and La-elements as dopants. Experimental results for solid solutions are included to provide demonstration of proof of principle for the theoretical model applied for 3D bulk structures. The maximum thermoelectric figure of merits of La$_x$Mg$_{2-x}$Si$_{0.49}$Ge$_{0.5}$Sb$_{0.01}$ solid solutions are obtained to be 0.64 and 0.56 at 800 K for $x = 0$ and $x = 0.01$ sample, respectively. While, at the same temperature, due to the relatively low phonon thermal conductivity the state-of-the-art *ZT* values of 2.41 and 2.26 have been attained in the Mg₂Si/Mg₂Ge/Mg₂Si quantum well samples with 0.01 wt. % Sb-doped and 0.01 wt. % Sb- and 0.01 wt. % La-doped, respectively. *Published by AIP Publishing.* [http://dx.doi.org/10.1063/1.4974463]

I. INTRODUCTION

In recent times, to develop alternative energy sources or energy recovery methods becomes our extremely urgent need because of the rising demand for energy and more importantly increasing concerns on global warming. In this sense, direct thermal-to-electric (or electric-to-thermal) energy conversion by using thermoelectric materials seems to be a possible solution to the current energy crisis and environmental problems.[1] Thermoelectric materials can be extensively used for potentially broad applications in refrigeration, waste heat recovery, solar energy conversion, etc.[1–5] The efficiency of a thermoelectric material is gauged by its dimensionless figure of merit $ZT = \frac{\sigma S^2}{\kappa_{total}}T$ which consists of a set of inter-related parameters; where S is the Seebeck coefficient, σ is the electrical conductivity and κ_{total} is the total thermal conductivity with κ_c is the carrier thermal conductivity (i.e., from electrons for n-type materials and from holes for p-type materials), κ_{bp} is the bipolar thermal conductivity (i.e., from electron-hole pairs) and κ_{ph} is the lattice thermal conductivity (i.e., from phonons). A desirable target for practical use of thermoelectric device is a value of $ZT > 1$ which leads to about 10% conversion efficiency.

The intermetallic compounds of Mg₂X (X = Si, Ge, and Sn) and their solid solutions have long been regarded as promising high-performance thermoelectric materials which are functional in the intermediate temperature range from 500 K to 900 K due to their large Seebeck coefficients, high electrical conductivities, and low thermal conductivities.[1] Mg₂X compounds are narrow band gap semiconductors and have a face-centered cubic lattice with antifluorite type structure with space group *Fm3m* with one molecular unit per primitive cell and four formulas per fcc conventional cell.[6] In the literature, sufficiently high values of thermoelectric figure of merit for these compounds and solid solutions are presented.[7–10] All these compounds are eco-friendly including no toxic components and have naturally abundant constituent elements which make them excellent candidates for large scale thermoelectric applications. While quite low *ZT* values were found for undoped Mg₂Si as $ZT = 0.04 - 0.06$ at nearly 750 K (Refs. 11–13) this could be significantly enhanced by doping with Sn, Ge, Sb, and Bi. As an example, very high value of thermoelectric figure of merit was gained for Mg₂Si$_{0.6}$Sn$_{0.4}$ as $ZT_{max} = 1.2$ at 700 K (Ref. 14) and for Mg₂Si$_{0.53}$Sn$_{0.4}$Ge$_{0.05}$Bi$_{0.02}$ as $ZT_{max} = 1.4$ at 823 K.[15]

In 1990s, nanostructured materials have been theoretically predicted to have considerably enhanced the thermoelectric efficiency compared to bulk materials,[16] and this prediction has also been experimentally confirmed in the cases of Bi₂Te₃/Sb₂Te₃ superlattices and PbTe quantum dots at 300 K with very high values of thermoelectric efficiencies as $ZT = 2.4$[17] and $ZT = 2$,[18] respectively. These findings have become the renaissance of thermoelectric materials and so motivated extensive studies on low dimensional semiconductors as thermoelectric materials. Significant improvements in thermoelectric efficiency by following this method mainly result from reducing the phonon thermal conductivity with the inclusion of additional interface scattering mechanisms. Particularly, the *ZT* values can be considerably enhanced by using nanostructured semiconductor alloys and their solid solutions since the mean-free paths of phonons (which are main heat carriers) in these systems are typically much

longer than the electronic mean-free paths. As reviewed above, bulk Mg_2X compounds and their solid solutions have significantly higher *ZT* values and proven to be the most appropriate thermoelectric materials in the intermediate temperature range with several advantages. However, thus far, there have been very scarce systematic theoretical and experimental studies of thermoelectric properties of Mg_2X based nanostructured systems. In this work, we first study the thermoelectric transport properties of Sn- and La-doped $Mg_2Si_{0.5}Ge_{0.5}$ solid solutions and compared our theoretical findings with the available experimental measurements done by Zhou *et al.*[19] Based on temperature dependent Fermi level calculation, the electronic transport properties (s, σ, and κ_c) are computed by following the Hicks and Dresselhaus' approach.[16] The temperature dependence of the thermal conductivity contributions from electron-hole pairs (κ_{bp}) and phonons (κ_{ph}) are computed by employing Price's theory[20] and Srivastava's scheme,[21] respectively. Phonon scattering rates including various types of scattering mechanisms are taken into account rigorously. By asking a key question is whether the *ZT* value of these solid solutions can be improved by nanostructuring, and by how much, we suggest Sb- and La-doped $Mg_2Si/Mg_2Ge/Mg_2Si$ quantum well systems. The calculation of temperature and well width dependence of thermoelectric transport properties of quantum well systems is done by applying a slight variation of Hicks and Dresselhaus' approach and for thermal conductivity, the additional interface mass-mixing scattering (ims) and interface dislocation scattering (ids) mechanisms are carried out by following the Yelgel and Srivastava's approach.[23] We will show that by making the quantum well structure of $Mg_2Si/Mg_2Ge/Mg_2Si$ with using the same type and amount of dopants as used in $Mg_2Si_{0.5}Ge_{0.5}$ solid solutions, the maximum value of *ZT* can be enhanced considerably. While for $Mg_2Si_{0.5}Ge_{0.5}Sb_{0.01}$ solid solution $ZT_{max,theo} = 0.64$ and $ZT_{max,expt} = 0.56$ at 800 K, its quantum well that forms with the well width of 10 nm has $ZT_{max,theo} = 2.41$ at the same temperature. Similarly, while $La_{0.01}Mg_2Si_{0.5}Ge_{0.5}Sb_{0.01}$ solid solution has $ZT_{max,theo} = 0.97$ and $ZT_{max,expt} = 0.96$ at 800 K, its quantum well structure with the well width of 10 nm has $ZT_{max,theo} = 2.26$ at the same temperature. The main reason for improving *ZT* with using quantum well systems is discussed in detail with including both temperature and well width dependencies of all thermoelectric transport properties for these systems.

II. THEORY

The thermoelectric figure of merit *ZT* has been calculated both for a three dimensional bulk material and a two dimensional quantum well structure. Calculations are for single band materials which are assumed to be the conduction band and also being different from several other studies where generally the constant relaxation time approximation is used, we prefer to use energy dependent relaxation time approximation.

A. Thermoelectric transport properties for a 3D bulk material

The methods for calculating Seebeck coefficient (S), electrical conductivity (σ), total thermal conductivity κ_{total} (including carrier thermal conductivity, κ_c, bipolar thermal conductivity, κ_{bp}, and lattice thermal conductivity, κ_{ph}) and hence *ZT* for both n- and p-type doped bulk semiconductors have already been described in our previous studies.[24,25] In these studies, since the parabolic bands are assumed, the electronic dispersion for 3D bulk systems is given as

$$\mathcal{E}_{3D}(k_x, k_y, k_z) = \frac{\hbar^2 k_x^2}{2m_x^*} + \frac{\hbar^2 k_y^2}{2m_y^*} + \frac{\hbar^2 k_x^2}{2m_z^*}, \tag{1}$$

where $\hbar$ is the reduced Planck's constant, k_x, k_y, and k_z are the propagation vector components and m_x^*, m_y^*, and m_z^* are the effective mass components along the axes x, y, and z, respectively.

1. Electronic transport properties

Starting from the temperature dependence of Fermi level in the extrinsic regime which is given as

$$E_{F,3D}^{ext} = \frac{1}{2}(E_c + E_d) + \frac{k_B T}{2} \ln \frac{N_d}{2U_c}$$
$$- k_B T \sinh^{-1} \left[\sqrt{\frac{U_c}{8N_d}} \exp\left(\frac{-\Delta E_i}{2k_B T}\right) \right], \tag{2}$$

where E_c is the conduction band edge, E_d is the donor energy level, N_d is the concentration of donor impurity atoms, $\Delta E_i = E_c - E_d$ is the donor ionisation energy, and $U_c = 2((m_n^* k_B T)/(2\pi\hbar^2))^{3/2}$ with m_n^* as the electron effective mass, and k_B is the Boltzmann constant,[26] the thermoelectric transport properties can be summarised as in the following forms (noted that in this work all studied samples only show extrinsic behaviour for the temperature range from 300 K to 800 K)

$$S_{3D} = \frac{k_B}{e}(\delta - \zeta^*), \tag{3}$$

$$\sigma_{ext,3D} = \frac{4}{3\pi\sqrt{\pi}} \frac{e^2}{m_c^*} \frac{\hbar\rho c_L^2}{E_D^2} F_{1/2}, \tag{4}$$

where c_L is the velocity of longitudinal phonons, ρ is the mass density, E_D is the deformation potential, the Fermi-Dirac function is written as $F_i = \int_0^\infty \frac{x^i dx}{e^{(x-\zeta^*)}+1}$ with e is the electron charge, $\zeta^* = E_f/k_B T$ is the reduced chemical potential, and $\delta = \frac{(r+\frac{5}{2})F_{r+\frac{3}{2}}(\zeta^*)}{(r+\frac{3}{2})F_{r+\frac{1}{2}}(\zeta^*)}$ where r is a scattering parameter.[16,27,28]

2. Thermal transport properties

The total thermal conductivity of semiconductor materials ($\kappa_{total} = \kappa_c + \kappa_{bp} + \kappa_{ph}$) has included three contributions from carriers (electrons for this study), electron-hole pairs (bipolar), and phonons, respectively. Expressions for these contributions can be written as

$$\kappa_{c,3D} = \left(\frac{k_B}{e}\right)^2 \sigma T \mathcal{L}_0, \tag{5}$$

$$\kappa_{bp,3D} = F_{bp} T^p \exp(-E_g/2k_B T), \tag{6}$$

where E_g is a band gap of a material, F_{bp} and p regarded as adjustable parameters and the Lorenz number for 3D bulk materials is given by[27]

$$\mathcal{L}_{0,3D} = \frac{\left(r+\frac{7}{2}\right)F_{r+\frac{5}{2}}(\zeta^*)}{\left(r+\frac{3}{2}\right)F_{r+\frac{1}{2}}(\zeta^*)} - \left[\frac{\left(r+\frac{5}{2}\right)F_{r+\frac{3}{2}}(\zeta^*)}{\left(r+\frac{3}{2}\right)F_{r+\frac{1}{2}}(\zeta^*)}\right]^2. \tag{7}$$

The phonon thermal conductivity is calculated by employing Debye's isotropic continuum model within the single-mode relaxation time approximation as[21]

$$\kappa_{ph,3D} = \frac{\hbar^2 q_D^5}{6\pi^2 k_B T^2} \sum_s c_s^4 \int_0^1 dx x^4 \tau \bar{n}(\bar{n}+1), \tag{8}$$

where τ is the phonon relaxation time, q_D is the Debye radius, $x = q/q_D$ is a reduced wavenumber, s represents the polarisation branch of phonon (longitudinal or transverse), $\bar{n}$ is the Bose-Einstein distribution function, and c_s is the velocity of phonons for polarisation branch s.

The phonon relaxation rate (τ^{-1}) is contributed by several scattering mechanisms: boundary scattering (bs), mass defects scattering (md), acoustic deformation scattering (dp), and anharmonic scattering (anh). By using the Matthiessen rule, the total effect of scattering processes is defined as $\tau^{-1} = \sum_i \tau_i^{-1}$, where τ_i^{-1} represents the contribution from ith scattering mechanism which can be summarised as the following forms.

a. Boundary scattering. The scattering of phonons with the boundaries of a sample is given by

$$\tau_{qs}^{-1}(bs) = \frac{c_s}{L}, \tag{9}$$

where L is a crystal size.[21,29]

b. Mass defect scattering. The scattering of phonons from isotopes and the effect of alloying in semiconductor alloys and compounds is written as[21,30]

$$\tau_{qs}^{-1}(md) = \frac{\Gamma_{md}\Omega}{4\pi\bar{c}^3} \omega^4(qs), \tag{10}$$

where Ω is the volume of a unit cell, $\bar{c}$ is the average phonon velocity, $\omega = cq$ and Γ_{md}, viz., $\Gamma_{isotopes}$ and Γ_{alloy} expressions have already been given in our previous study.[24]

c. Acoustic deformation potential scattering. The relaxation time for the interaction of the charge carriers (electrons for present study) with acoustic mode phonons is expressed as[31]

$$\tau_{ql}^{-1}(dp) = \frac{3}{8\sqrt{\pi}} \frac{E_{df}^2}{\rho c_L^2 \hbar^4} \left(2m_p^* k_B T\right)^{3/2}. \tag{11}$$

where E_{df} is a scaled deformation potential.

d. Anharmonic phonon scattering. By restricting ourselves to only three-phonon processes and following Srivastava's scheme[21] the phonon-phonon scattering mechanism is given by

$$\tau_{qs}^{-1}(anh) = \frac{\hbar q_D^5 \gamma^2}{4\pi\rho\bar{c}^2} \sum_{s's''\varepsilon} \left[\int dx' x'^2 x''_+ [1-\varepsilon+\varepsilon(Cx+Dx')] \right.$$
$$\times \frac{\bar{n}_{q's'}(\bar{n}''_+ + 1)}{(\bar{n}_{qs}+1)} + \frac{1}{2}\int dx' x'^2 x''_- [1-\varepsilon$$
$$\left. + \varepsilon(Cx - Dx')] \frac{\bar{n}_{q's'}\bar{n}''_-}{\bar{n}_{qs}} \right], \tag{12}$$

where γ is the Grüneisen constant, $x' = q'/q_D$, $x''_+ = Cx \pm Dx'$, $\bar{n}''_\pm = \bar{n}(x''_\pm)$, $C = c_s/c_{s''}$, $D = c_{s'}/c_{s''}$. $\varepsilon = 1$ for momentum-conserving (Normal) processes, and $\varepsilon = -1$ for momentum-nonconserving (Umklapp) processes. The first and second terms in Eq. (12) are controlled by class 1 events ($qs + q's' \rightarrow q''s''$) and class 2 events ($qs \rightarrow q's' + q''s''$), respectively. The integration limits on the variables x and x', have already been derived from a detailed consideration of the energy and momentum conservation requirements given in Ref. 21.

B. Thermoelectric transport properties for a 2D quantum well

Quantum wells are layered structures which utilize the band gap differences between materials A and B to confine the current carriers to the well in layer A. The schematic of this layered structure is given in Fig. 1. The region of width d_A is the quantum well which conducts electricity and the region of width d_B is the barrier region which is nonconducting and serves to confine the carriers (which are electrons for present work) to the quantum wells. For current study the material A is Mg$_2$Ge, and the material B is Mg$_2$Si with the indirect energy band gaps of 0.74 eV and 0.77 eV at 0 K, respectively.[22]

For the theoretical modelling of the quantum well system with negligible barrier width ($d_B \simeq 0$), we simply assume the parabolic energy bands for electrons in the conduction bands with occupying only the lowest sub-band ($j = 1$). Accordingly, for quantum confinement in z direction (means that quantum well system grown in z direction) the electronic dispersion relation is given by

$$\mathcal{E}_{2D}(k_x, k_y) = \frac{\hbar^2 k_x^2}{2m_x^*} + \frac{\hbar^2 k_y^2}{2m_y^*} + E_j, \tag{13}$$

where E_j is the jth quantum sublevel given by

$$E_j = \frac{\hbar^2 \pi^2}{2m_z^* d_A^2} j. \tag{14}$$

The effective mass tensor components of the constant energy surfaces for well material are denoted as m_x^*, m_y^*, and m_z^*. Due to the lack of experimental values of effective mass tensors for Mg$_2$Ge quantum well material, we computationally
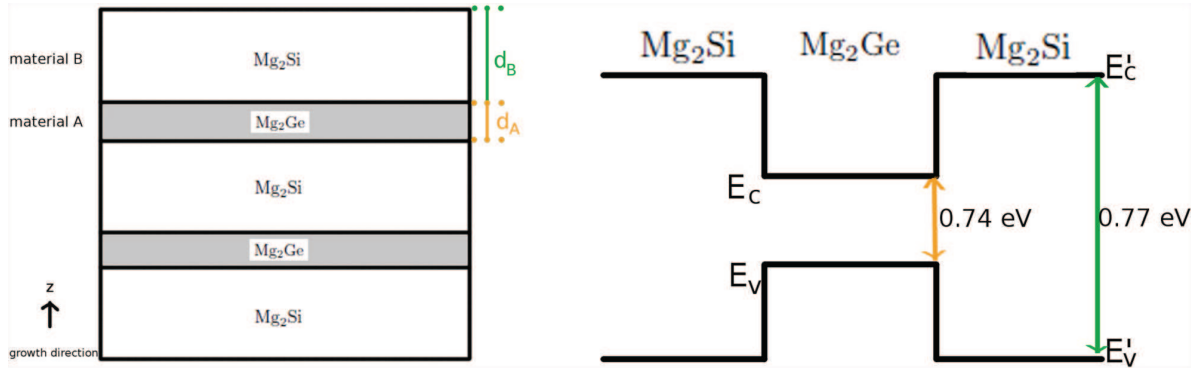
FIG. 1. Schematic cross section of $Mg_2Si/Mg_2Ge/Mg_2Si$ quantum well structure. The wells have a thickness d_A and the barriers have a thickness d_B. At 0 K, the indirect band gaps were found to be $E_g(Mg_2Ge) = 0.74$ eV and $E_g(Mg_2Si) = 0.77$ eV.[22]

calculated these values by using the density functional theory (DFT) and found the same value of $0.253\, m_e$ for all diagonal tensor components where m_e is the mass of electron. Additionally, the details of this calculation can be found in the Appendix section.

1. Electronic transport properties

Thermoelectric transport properties of quantum well systems are defined within the single-band nearly free-electron consideration in the $x-y$ plane and to calculate these in-plane transport properties, we need to first calculate the temperature dependence of Fermi level in the extrinsic regime which is given as[23]

$$
E_{\mathrm{F},2D}^{\mathrm{ext}} = \frac{1}{2}(E_c + E_d) + \frac{k_B T}{2}\ln\frac{N_d}{2U_c}
$$
$$
- k_B T \sinh^{-1}\left[\sqrt{\frac{U_c}{8N_d}}\exp\left(\frac{-\Delta E_i^{(n)}}{2k_B T}\right)\right] - \frac{\hbar^2\pi^2}{2m_z^* d_A^2}j.
\tag{15}
$$

Expressions of in-plane transport properties of quantum well systems can be written in the following forms:

$$
S_{2D} = \pm\frac{k_B}{e}\left[\frac{(2+r)F_{1+r}}{(1+r)F_{0+r}} - \zeta^*\right],
\tag{16}
$$

$$
\sigma_{\mathrm{ext},2D} = \frac{4}{3d_A}\frac{\hbar^2\rho c_L^2}{\sqrt{2\pi}}\frac{e^2}{m_x^*\sqrt{m_z^*}}\frac{F_0}{E_D^2(k_B T)^{1/2}}.
\tag{17}
$$

2. Thermal transport properties

Thermal conductivity contributions for quantum well systems can be summarised as in the following forms:

$$
\kappa_{c,2D} = \left(\frac{k_B}{e}\right)^2 \sigma T \mathcal{L}_0,
\tag{18}
$$

where the Lorenz number for 2D systems is expressed as

$$
\mathcal{L}_0 = \frac{(3+r)F_{2+r}}{(1+r)F_{0+r}} - \left[\frac{2+r}{1+r}\frac{F_{1+r}}{F_{0+r}}\right]^2.
\tag{19}
$$

The bipolar thermal conductivity of a quantum well system is calculated by using the same expression for 3D bulk systems given in Eq. (6), the only difference with using the band gap of quantum well (QW) system given as

$$
E_g(\mathrm{QW}) = E_c - E_v + \frac{\hbar^2\pi^2}{2m_z^* d_A^2}.
\tag{20}
$$

By employing Debye's isotropic continuum approximation within the single-mode relaxation time scheme, the lattice thermal conductivity of a bulk material has already been expressed in Eq. (8). By following the same scheme for 2D quantum well systems, the phonon scattering rates from sample boundaries and acoustic deformation potential can be used as same as 3D bulk systems which have already been given in Eqs. (9) and (11). More importantly additional to these scattering mechanisms, we need to focus on two additional considerations for interface mass-mixing scattering (ims) resulting from diffusion or mixing of atoms at the interfaces and interface dislocation scattering (ids) arising from dislocations or missing bonds.

a. Interface mass-mixing scattering rate. At quantum well interfaces, mass-mixing arising from diffusion or mixing of atoms can be given as[23]

$$
\tau_{qs}^{-1}(\mathrm{ims}) = \frac{\Gamma_{\mathrm{ims}}\Omega}{4\pi\bar{c}^3}\omega^4(qs),
\tag{21}
$$

with the mass-mixing parameter for a QW system given as

$$
\Gamma_{\mathrm{ims}} = \frac{2\beta_0}{(n+m)}\sum_i\exp\left(-\left|\frac{l_i - l_0}{d}\right|\right)\left(\frac{\Delta M_i}{\bar{M}}\right)^2
$$
$$
\times\left[\left(1-\frac{e_A^2}{e_B^2}\right)^2 + \left(1-\frac{e_B^2}{e_A^2}\right)^2\right],
\tag{22}
$$

where d is the interlayer distance (d_A in the well and d_B in the barrier), l_i is the layer distance from interface, l_0 is the z coordinate of the interface, β_0 is the mass-mixing fraction at

the interface, and e_B/e_A is the ratio of the amplitudes of eigenvectors in materials B and A.

b. Interface dislocation scattering. Interface dislocation scattering results from the broken bonds (especially the lines of broken bonds) close to the interface, and this scattering rate can be defined as[23]

$$\tau_{qs}^{-1}(\text{ids}) = \frac{\Gamma_{\text{ids}}\Omega}{8\pi\bar{c}^3}\omega_0^4, \qquad (23)$$

where ω_0 can be approximated as the highest zone-centre frequency ($\omega_0 = \omega_D = \bar{c}.q_D$) and the interface dislocation parameter is written as

$$\Gamma_{\text{ids}} = \frac{2\beta_0'}{(n+m)}\sum_i \exp\left(-\left|\frac{l_i - l_0}{d}\right|\right)\left(\frac{\Delta M_i}{\bar{M}}\right)^2$$
$$\times \left[1 + \left(\frac{e_A^2}{e_B^2}\right)^2 + 1 + \left(\frac{e_B^2}{e_A^2}\right)^2\right], \qquad (24)$$

with β_0' being the fraction of broken bonds in the interface region.

The amplitude ratio e_B/e_A required for both interface mass-mixing and dislocation scattering mechanisms is approximated using the diatomic linear chain model along the growth direction as

$$\frac{e_B}{e_A} = \frac{\left[\frac{1}{M_0} - \Delta\left(\frac{1}{M}\right)\right]\cos(l_z q_z)}{\left\{\left(\frac{1}{M_0}\right)^2 \cos^2(l_z q_z) + \left[\Delta\left(\frac{1}{M}\right)\right]^2 \sin^2(l_z q_z)\right\}^{1/2} - \Delta\left(\frac{1}{M}\right)}, \qquad (25)$$

with $1/M_0 = \frac{1}{2}(1/M_A + 1/M_B)$, $\Delta(1/M) = \frac{1}{2}(1/M_A - 1/M_B)$ and $l_z = d_A + d_B$ is the period along the growth direction.

c. Anharmonic phonon scattering. For the materials containing only one atom per primitive unit cell, namely, for bulk systems, we define the anharmonic scattering mechanism with Eq. (12). When the number of atoms increases in a unit cell, this equation should be re-written owing to an increased amount of anharmonic scattering strength. In our previous work[23] by following the discussions given in Refs. 32 and 33, we modelled the anharmonic phonon scattering rate for quantum well systems as

$$\tau_{qs}^{-1}(\text{anh}, \text{QW}) = \tau_{qs}^{-1}(\text{anh}, \text{bulk})(n_A + n_B)^{2/3}, \qquad (26)$$

with n_A and n_B are being the number of well layers and barrier layers, respectively.

III. RESULTS AND DISCUSSION

A. Thermoelectric properties of 3D bulk Sb- and La-doped Mg₂Si₀.₅Ge₀.₅ solid solutions

All related parameters for the calculation of thermoelectric properties of Sb- and La-doped $Mg_2Si_{0.5}Ge_{0.5}$ solid solutions are listed in Table I. All integrals are evaluated by using Simpson's rule. Related experimental measurements are read from the work of Zhou *et al.*[19]

The temperature dependence of Fermi level for $La_xMg_{2-x}Si_{0.49}Ge_{0.5}Sb_{0.01}$ solid solutions with $x=0$ and $x=0.01$ is presented in Fig. 2(a). For both samples only the extrinsic behaviour is observed from $300\,\text{K}$ to $800\,\text{K}$. This can also be verified from the experimental measurements of the Seebeck coefficient done by Zhou *et al.*[19] They did not get any extrinsic-to-intrinsic-turn-over behaviour in S–T variation for the entire temperature range. Also, it is found that

with including both Sb- and La-dopants on $Mg_2Si_{0.5}Ge_{0.5}$ solid solution, both the electron effective mass and carrier concentration increase which suggests that the band structure is modified by these dopants in particular, the conduction band. Moreover, as seen from Fig. 2(a), our theoretical Fermi level gently improves with an additional doping level due to simultaneous increments in m_n^* and/or N_d.

Figure 2(b) shows the Seebeck coefficient-temperature variation for both types of doped solid solutions including

TABLE I. Properties and parameters used in the calculations of thermoelectric properties of bulk $La_xMg_{2-x}Si_{0.49}Ge_{0.5}Sb_{0.01}$ with $x=0$ and $x=0.01$ solid solution series.

| Property/parameter	0La	0.01La
$E_g(0)$ (eV)[36]	0.755	0.755
E_d (eV)	0.14	0.13
α (eV/K)	0.000885	0.000885
N_d (m⁻³)[19]	0.82×10^{25}	6.98×10^{25}
m_n^*/m_e^* (Ref. 19)	0.31	0.84
m_p^*/m_e^*	0.34	0.92
r	-0.5	-0.5
ρ (kg/m³)[36]	2.485×10^3	2.485×10^3
c_L (m/s)[36]	6.975×10^3	6.975×10^3
c_T (m/s)[36]	4.375×10^3	4.375×10^3
E_D (eV)	8.265	8.265
A (K⁻¹·¹)	0.008	0.022
a_{lat} (Å)[36]	6.364	6.364
ς	1.1	1.1
F_{bp} (W m⁻¹ K⁻²)	0.1×10^{-4}	0.1×10^{-4}
q_D (Å⁻¹)[36]	0.972	0.972
L (mm)	0.2	0.2
Ω (Å³)	64.45	64.45
Γ_{md}	23.0×10^{-4}	38.3×10^{-4}
E_{df} (eV)	3.45	1.3
γ	1.4	1.4
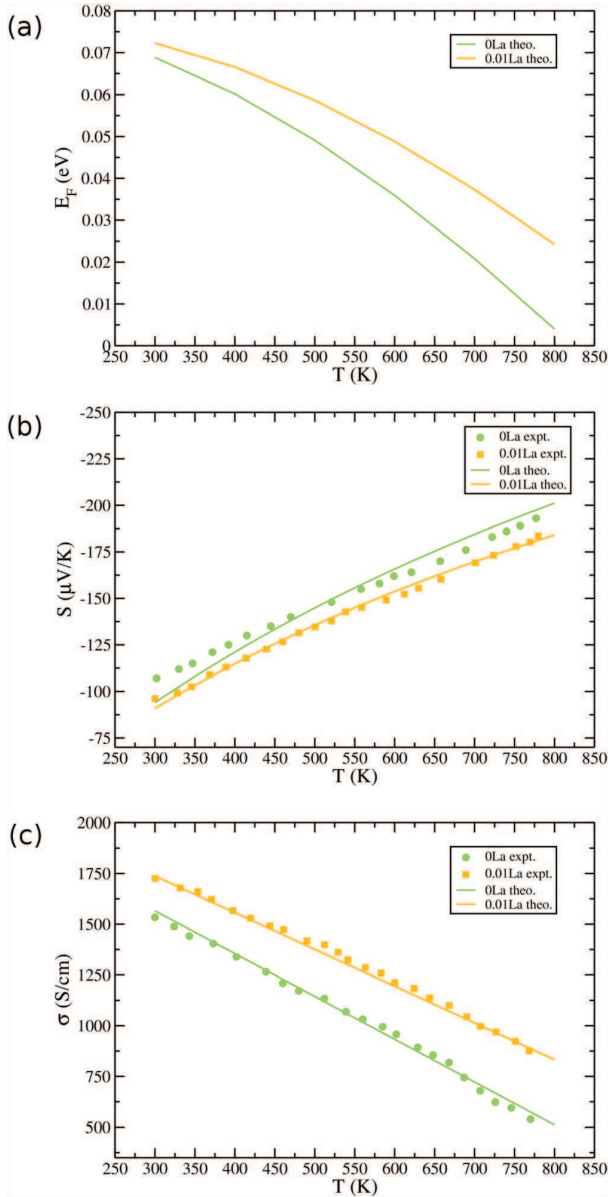
FIG. 2. Temperature dependence of electronic transport properties (a) the Fermi level, (b) the Seebeck coefficient, and (c) the electrical conductivity of $La_xMg_{2-x}Si_{0.49}Sb_{0.01}$ where $x = 0$ and $x = 0.01$. Solid lines are our theoretical calculations, and the symbols are the experimental measurements read from Ref. 19.

their experimental measurements read from Ref. 19. Both theoretical and experimental negative values of S support the n-type doping by using Sb and La elements as dopants on $Mg_2Si_{0.5}Ge_{0.5}$. As seen in Fig. 2(b), due to the extrinsic behaviour of these samples, S increases with temperature throughout the temperature range. Moreover, in consistence with Eq. (3), the $|S|$ decreases with increasing La concentration which is sourced from increasing electron effective mass. At 800 K, the maximum $|S|$ values are theoretically found to be as 201.11 μV/K and 184.03 μV/K for $x = 0$ sample and $x = 0.01$ sample, respectively. While their experimental maximum were measured to be 193.47 μ/K at 777 K for $x = 0$ sample and 183.57 μ/K at 779 K for $x = 0.01$ sample.

In Fig. 2(c), the temperature behaviour of electrical conductivity for both solid solutions is presented including their experimental values read from Ref. 19. In addition to the electrical conductivity expression given in Eq. (4) where only electron-acoustic phonon scattering is taken into account, there is also the supplement scattering mechanisms sourced from optical phonons, neutral impurities, ionized impurities, and alloying. Thus we can scale the electrical conductivity as[24]

$$\sigma_{3D} = \sigma_{ext,3D}AT^{\varsigma}, \qquad (27)$$

with A and ς are adjustable parameters. The electrical conductivity increases with additional dopants because of rising m_n^* and/or N_d. At 300 K, the maximum electrical conductivity values are found to be; $\sigma_{theo}(0La) = 1565.66$ S cm^{-1} and $\sigma_{theo}(0.01La) = 1737.65$ S cm^{-1} where their experimental maximum values at the same temperature were found to be as $\sigma_{expt}(0La) = 1534.88$ S cm^{-1} and $\sigma_{expt}(0.01La) = 1725.33$ S cm^{-1},[19] respectively.

In Fig. 3(a), the theoretical calculation of the carrier thermal conductivity for both types of doped solid solutions is presented as temperatures from 300 K to 800 K. As expected from the Wiedemann-Franz law, larger κ_c is gained while the doping level increases since $\kappa_c \propto \sigma$.

In Fig. 3(b), temperature dependence of the sum of bipolar and phonon thermal conductivity is displayed for both solid solutions including their experimental values read from Ref. 19. From our theoretical calculations, we note that for both samples, the bipolar contribution starts to become visible nearly at 800 K this is why we cannot see the significant contribution on to $T - (\kappa_{ph} + \kappa_{bp})$ variation. Also this becomes the evidence of samples' extrinsic behaviour for the studied temperature range. From our theoretical $\kappa_{bp} + \kappa_{ph}$ calculations, we conclude the following; at low temperature ($T < 100$ K) only the boundary and acoustic deformation potential scattering becomes dominant, at high temperature ($T > 100$ K) only the anharmonic scattering becomes dominant, for throughout the temperature range, the mass defect scattering plays a major role on κ_{ph}. In consistence with these theoretical findings, in Fig. 3(b), for both samples it is clearly seen that $\kappa_{ph} + \kappa_{bp}$ mostly shows only the κ_{ph} behaviour from 300 K to 800 K. Both experimentally and theoretically, a very slight increment in $\kappa_{ph} + \kappa_{bp}$ results can be observed near 800 K for both solid solutions owing to a very little contribution sourced from the bipolar scattering. Moreover, it is seen both theoretically and experimentally that as we increase the value of x due to the increasing mass defect scattering mechanism (as defined with the parameters of Γ_{md} in Table I) $\kappa_{ph} + \kappa_{bp}$ decreases systematically.

Finally, the temperature behavior of total thermal conductivity for both solid solutions is represented in Fig. 3(c) including their experimental measurements read from Ref. 19. Both experimentally and theoretically, it is proven that with additional doping, the phonon thermal conductivity can be reduced effectively and leads to lower total thermal conductivity. For $x = 0$ sample, the theoretical minimum of κ_{total} is found to be $\kappa_{total,theo}(0La) = 3.27$ W/m K at 600 K while its experimental minimum was $\kappa_{total,expt}(0La) = 3.30$ W/m K at 651 K. For $x = 0.01$ it is theoretically found that $\kappa_{total,theo}(0.01La) = 2.24$ W/m K at 800 K while it was experimentally gained to be $\kappa_{total,expt}(0.01La) = 2.21$ W/m K at 772 K.
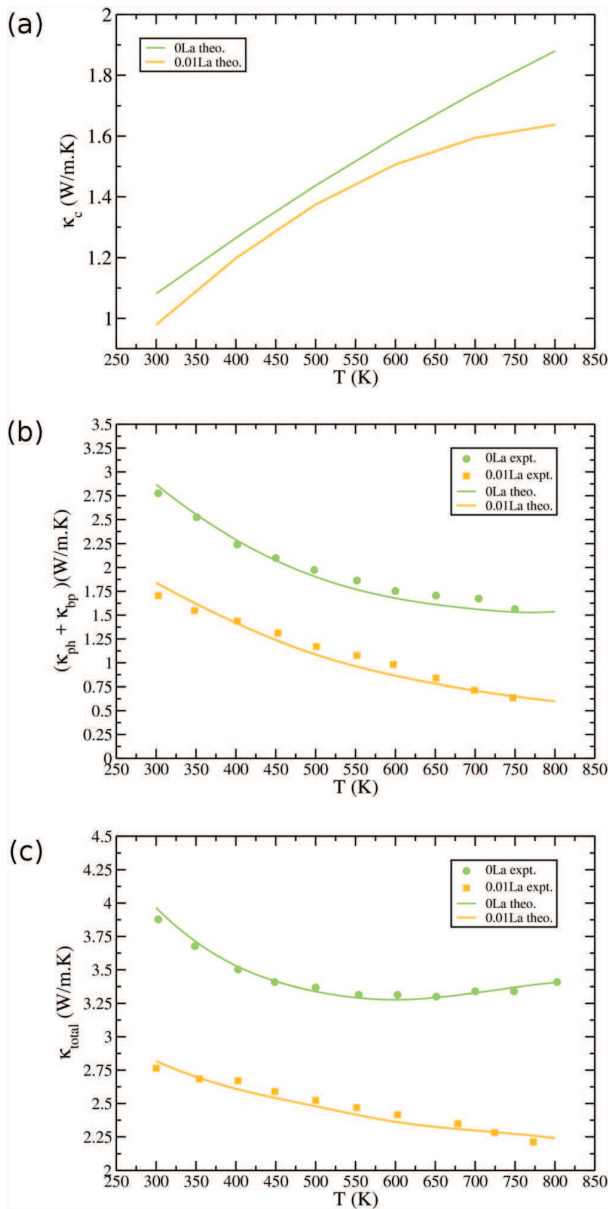
FIG. 3. Temperature dependence of thermal transport properties (a) carrier thermal conductivity, (b) the sum of phonon and bipolar thermal conductivity, and (c) the total thermal conductivity of $La_xMg_{2-x}Si_{0.49}Sb_{0.01}$ where $x = 0$ and $x = 0.01$. Solid lines are our theoretical calculations, and the symbols are the experimental measurements read from Ref. 19.

In Fig. 4, $ZT - T$ variation is represented both theoretically and experimentally. For both samples owing to only extrinsic behaviour, ZT goes up with temperatures for the entire temperature range. Our theoretical results are in a very good agreement with the experimental measurements. For $x = 0$ sample, the maximum value of ZT is theoretically obtained to be $ZT_{theo}(0La) = 0.64$ at 800 K while it was experimentally found to be $ZT_{expt} = 0.56$ at 750 K. For $x = 0.01$ sample, theoretically, we found the maximum thermoelectric efficiency value as $ZT_{theo}(0.01La) = 0.97$ at 800 K whereas it was experimentally measured as $ZT_{expt} = 0.96$ at 798 K. To summarise, comparing these two samples with
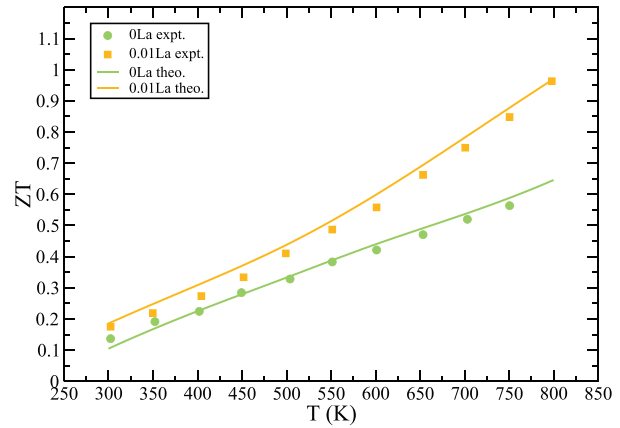
FIG. 4. Temperature dependence of thermoelectric figure of merit ZT of $La_xMg_{2-x}Si_{0.49}Sb_{0.01}$ where $x = 0$ and $x = 0.01$. Solid lines are our theoretical calculations, and the symbols are the experimental measurements read from Ref. 19.

considering their theoretical ZT values, increasing the doping level with $x = 0.01$, thermoelectric efficiency can be enhanced by 51% at 800 K whereas it was experimentally found to be 71% by Zhou et al.[19] The reason for this difference is that it mainly comes from our slightly higher theoretical $|S|$ values gained for $x = 0$ solid solution compared to its experimental results.

B. Thermoelectric properties of Sb- and La-doped 2D Mg$_2$Si/Mg$_2$Ge/Mg$_2$Si quantum well systems

For Mg$_2$Si/Mg$_2$Ge/Mg$_2$Si quantum well systems, the doping levels are considered to be the same as $Mg_{2-x}Si_{0.5}Ge_{0.5}$ solid solutions studied above. The first type of Mg$_2$Si/Mg$_2$Ge/Mg$_2$Si quantum well is doped with only 0.01 wt. % Sb without La doping (which will be called as 0La QWs) and the second type of Mg$_2$Si/Mg$_2$Ge/Mg$_2$Si quantum well is doped with both 0.01 wt. % Sb and 0.01 wt. % La (which will be called as 0.01La QWs). These quantum well systems will be studied in the well width values chosen as $d_A = 10$ nm, 15 nm, and 20 nm, respectively. The well width range is made by considering that below the critical d_A value, the lowest bound state in the conduction band increases above the highest bound state in the valence band and causes a semimetal-semiconductor transition.[34,35] Therefore, for both types of quantum well systems, the lowest value of well widths are found to be $d_A = 10$ nm. All related parameters for the calculation of thermoelectric properties of Sb- and La-doped Mg$_2$Si/Mg$_2$Ge/Mg$_2$Si quantum well systems are listed both in Tables I and II. Owing to the same level of Sb- and La-dopings on Mg$_2$Si/Mg$_2$Ge/Mg$_2$Si quantum wells, several parameters can be taken to be the same as their bulk values. Thus, quantum well parameters which are not listed in Table II should be considered as same as their bulk values.

In Figs. 5(a) and 5(b), the temperature variation of E_F is represented for both quantum well systems. As observed in their bulk forms in Sec. III A all considered quantum well systems show only an extrinsic behavior throughout the temperature range thus the extrinsic-to-intrinsic-turn-over behavior cannot be observed. In Figs. 5(c) and 5(d), the well

TABLE II. Parameters used in the calculations of thermoelectric properties of Sb-doped (with 0.01 wt. % Sb and 0 wt. % La) and La-doped (both with 0.01 wt. % Sb and 0.01 wt. % La) $Mg_2Si/Mg_2Ge/Mg_2Si$ quantum well systems with well width values that are taken as $d_A = 10$ nm, 15 nm, and 20 nm, respectively.

	0La QWs			0.01La QWs		
Property/parameter	10 nm	15 nm	20 nm	10 nm	15 nm	20 nm
E_g (eV)	0.755	0.746	0.743	0.755	0.746	0.743
E_{conf} (eV)	0.015	0.006	0.003	0.015	0.006	0.003
n_A	15	23	31	15	23	31
$\Gamma_{ims} \times 10^{-4}$	8.10	8.10	8.10	13.44	13.44	13.44
$\beta_0 = \beta'_0$	0.5	0.5	0.5	0.5	0.5	0.5

width dependence of E_F is presented for both quantum wells at different temperatures. As can be easily expected from Eq. (15), for both types of doped quantum wells, the E_F decreases with reducing well width d_A at all temperatures.

The temperature dependence of the Seebeck coefficient of both types of quantum wells are shown in Figs. 6(a) and 6(b) for several well widths. For all quantum well systems, the n-type doping can be readily confirmed with negative S values. For both types of quantum wells owing to only

extrinsic behavior $|S|$ increases with the temperature throughout the temperature range. Moreover, in Figs. 6(c) and 6(d), it is seen that for both types of doped quantum well systems by following Eq. (16), increasing quantum well widths lead to slight reduction in $|S|$ at all selected temperatures. At 800 K, the maximum value of $|S|$ is found to be 214.49 μV/K and 196.45 μV/K for 0La doped and 0.01La doped quantum well systems, respectively.

Temperature dependent electrical conductivities are displayed in Figs. 7(a) and 7(b) for both types of quantum well systems with different well widths. Similar to the bulk solid solutions for the calculation of electrical conductivity of quantum well systems, additional scattering mechanisms are being taken into account as defined in Eq. (27) with the same A and ς adjustable parameters taken for bulk samples. Thus as found for bulk solid solutions, σ reduces with temperatures for all quantum well systems. Additionally, as seen in Figs. 7(c) and 7(d), higher σ values are gauged theoretically for smaller d_A values in accordance with Eq. (17). At room temperature, the maximum σ values are theoretically gained for $d_A = 10$ nm quantum wells as 917.96 S/cm and 2660.19 S/cm for 0La and 0.01La quantum wells, respectively.

In Figs. 8(a) and 8(b), the temperature variation of carrier thermal conductivity for both types of quantum well
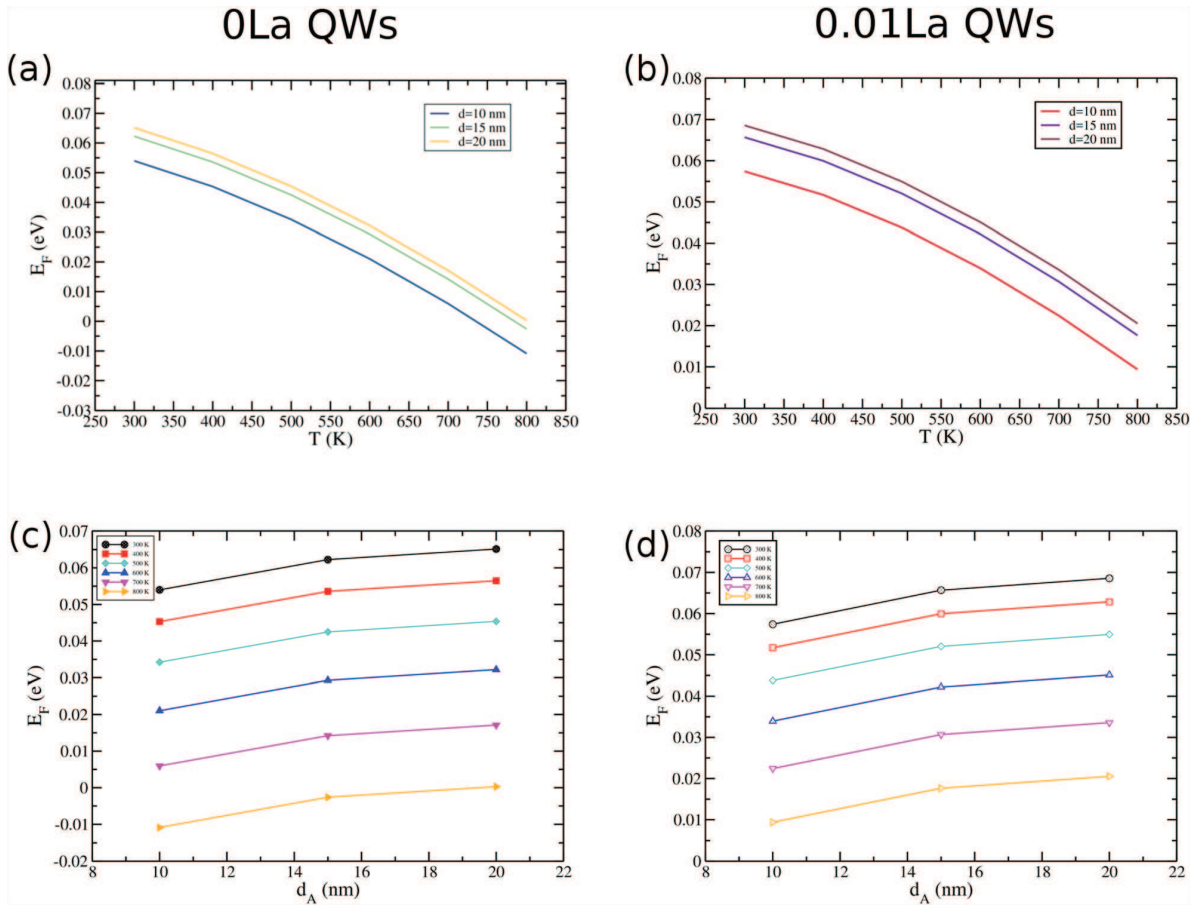

FIG. 5. Temperature dependence of the Fermi level for doped $Mg_2Si/Mg_2Ge/Mg_2Si$ quantum wells with different well widths (chosen as $d_A = 10$ nm, 15 nm, and 20 nm) (a) for 0La quantum wells (where the doping level as 0.01 wt. % Sb and 0 wt. % La) and (b) for 0.01La quantum wells (where doping levels as 0.01 wt. % Sb both with 0.01 wt. % La). The well width dependence of the Fermi level (c) for 0La QWs and (d) for 0.01La QWs.
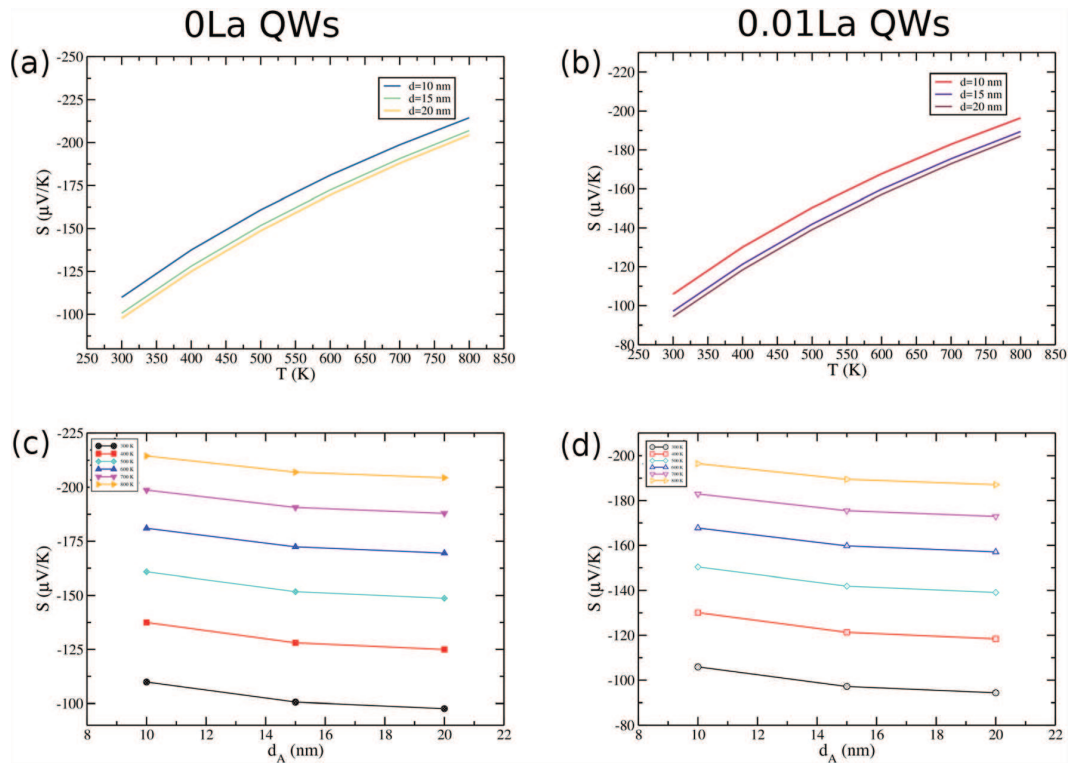
FIG. 6. Temperature dependence of the Seebeck coefficient for doped $Mg_2Si/Mg_2Ge/Mg_2Si$ quantum wells with different well widths (chosen as $d_A = 10$ nm, 15 nm, and 20 nm) (a) for 0La QWs and (b) for 0.01La QWs. The well width dependence of the Seebeck coefficient (c) for 0La QWs and (d) for 0.01La QWs.
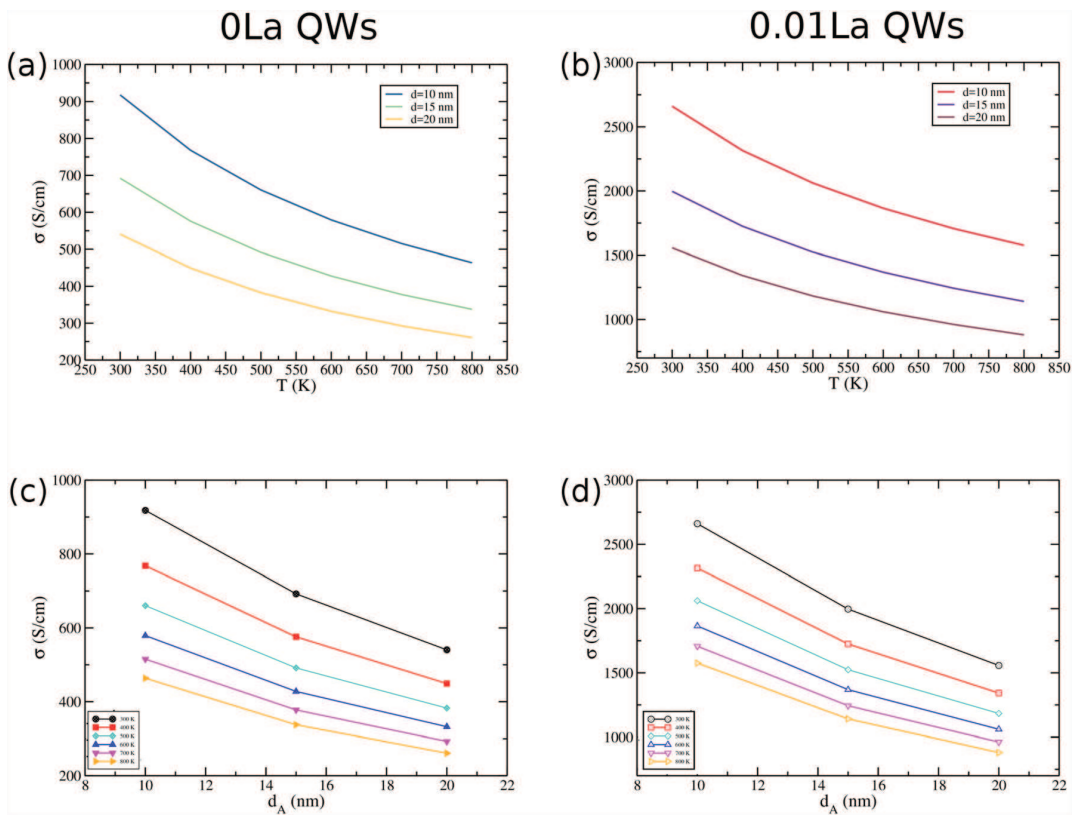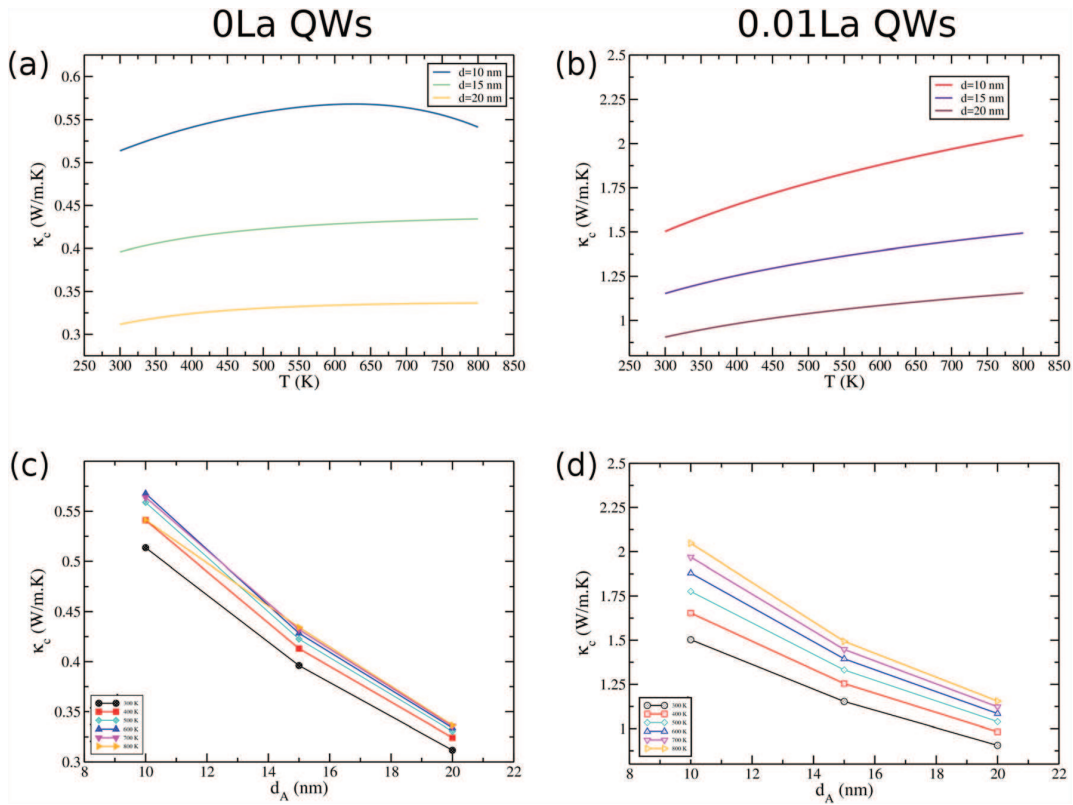

FIG. 7. Temperature dependence of the electrical conductivity for doped $Mg_2Si/Mg_2Ge/Mg_2Si$ quantum wells with different well widths (chosen as $d_A = 10$ nm, 15 nm, and 20 nm) (a) for 0La QWs and (b) for 0.01La QWs. The well width dependence of the electrical conductivity (c) for 0La QWs and (d) for 0.01La QWs.

FIG. 8. Temperature dependence of the carrier thermal conductivity for doped Mg$_2$Si/Mg$_2$Ge/Mg$_2$Si quantum wells with different well widths (chosen as $d_A = 10$ nm, 15 nm, and 20 nm) (a) for 0La QWs and (b) for 0.01La QWs. The well width dependence of the carrier thermal conductivity (c) for 0La QWs and (d) for 0.01La QWs.

systems are displayed with different well widths. As found for electrical conductivity calculation with compatibility, the Wiedemann Franz law increasing the doping level leads to an enhancement in κ_c for all studied quantum well systems. Additionally, from Figs. 8(c) and 8(d), it is shown that as the well width becomes larger, the value of κ_c decreases for both types of quantum well systems which can be expected from the σ-d_A calculation given in the above.

The sum of bipolar and phonon thermal conductivity versus temperature calculation is represented in Figs. 9(a) and 9(b) for both types of quantum well systems. While due to the bipolar conduction, we observed a slight increment in $\kappa_{bp} + \kappa_{ph}$ for La$_x$Mg$_{2-x}$Si$_{0.49}$Ge$_{0.5}$Sb$_{0.01}$ solid solutions we cannot see this trend for the studied quantum well systems. This means that with using low dimensional form of La$_x$Mg$_{2-x}$Si$_{0.49}$Ge$_{0.5}$Sb$_{0.01}$ solid solution, the bipolar contribution on thermal conductivity can be neglected at the studied temperature range. Also it should be noted that for quantum well structures while κ_{bp} is dependent on $E_g(QW)$, the electronic properties (E_F, S, and σ) depend on both doping level and the confinement energy $\hbar^2\pi^2/2m_z^*d_A^2$. For all quantum well samples from the theoretical calculation of $\kappa_{bp} + \kappa_{ph}$, we can note that: boundary and deformation-phonon scattering rates play a major role for the κ_{ph}-T relationship at low temperatures ($T < 100$ K), mass defect scattering is important at both low and high temperatures (below and above 100 K) and three-phonon interactions

become dominant only at high temperatures ($T > 100$ K). Besides these scattering mechanisms for all quantum wells, it is found that the interface dislocation scattering has a very small effect on κ_{ph} for $T < 100$ K on the contrary, the interface mass-mixing scattering has a very significant effect on κ_{ph} for $T > 100$ K. Owing to additional interface scattering mechanisms and scaled phonon-phonon interaction, all quantum well systems have smaller κ_{ph} value than their bulk form. The significant reduction is the most desired condition to have an enhanced value of ZT. Moreover, in Figs. 9(c) and 9(d), it is seen that for both types of quantum well systems $\kappa_{bp} + \kappa_{ph}$ noticeably decreases with lowering the quantum well width d_A. From this calculation, we can conclude that the most dominant scattering mechanism on κ_{ph} is coming from the anharmonic interaction since $\tau^{-1}(qs) \propto d_A$ whereas interface mass-mixing and dislocation scatterings $\propto \frac{1}{d_A}$. Thus the minimum values of $\kappa_{bp} + \kappa_{ph}$ are gained for the quantum well systems with the well width of 10 nm and for 0La doped quantum well system, it is obtained as 0.11 W/m K at 800 K whereas we theoretically found its bulk form value as 1.53 W/m K at the same temperature. Also, for 0.01La doped quantum well system, the minimum $\kappa_{bp} + \kappa_{ph}$ value is found to be 0.09 W/m K while its bulk has the value of 0.59 W/m K at 800 K. Hereby with these huge drop-offs in $\kappa_{bp} + \kappa_{ph}$, we can readily expect the significant enhancements in thermoelectric efficiencies of studied quantum well structures compared to their bulk solid solutions.
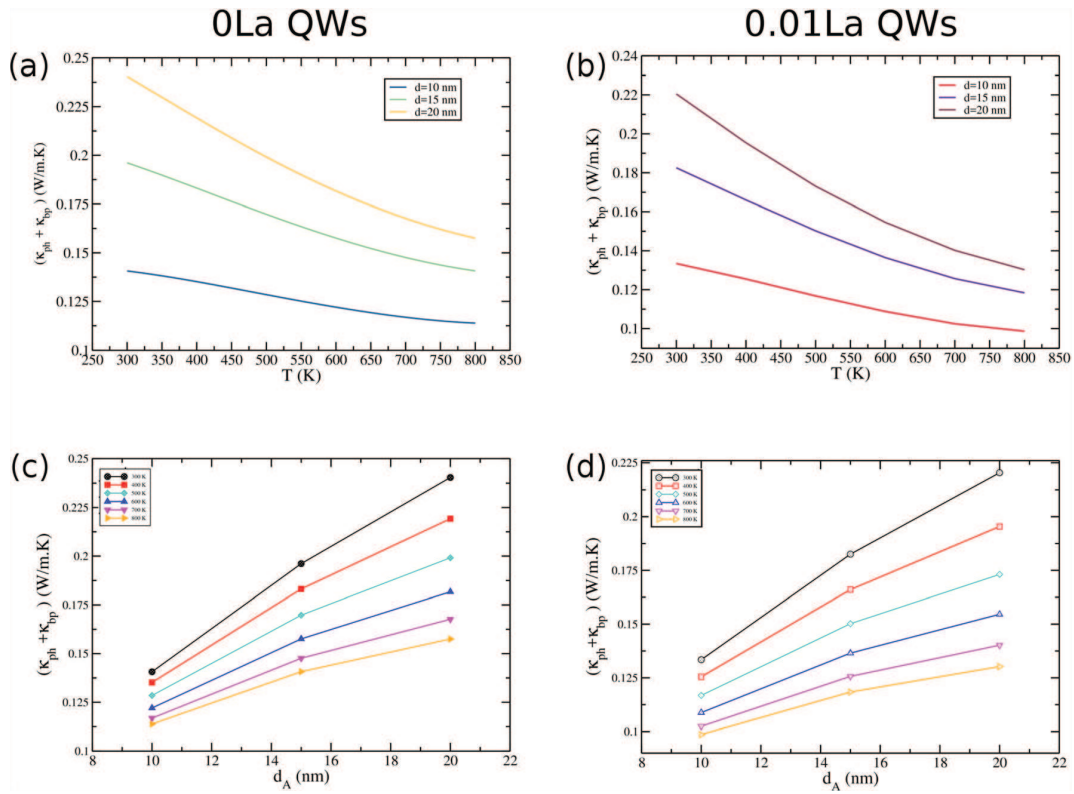
FIG. 9. Temperature dependence of the sum of phonon and bipolar thermal conductivity for doped $Mg_2Si/Mg_2Ge/Mg_2Si$ quantum wells with different well widths (chosen as $d_A = 10$ nm, 15 nm, and 20 nm) (a) for 0La QWs and (b) for 0.01La QWs. The well width dependence of the sum of phonon and bipolar thermal conductivity (c) for 0La QWs and (d) for 0.01La QWs.

The temperature dependence of total thermal conductivity is represented in Figs. 10(a) and 10(b) for 0La and 0.01La quantum well systems with different well widths, respectively. Due to its higher carrier thermal conductivity values larger κ_{total} values are gained for 0.01La doped quantum well systems compared to 0La doped quantum well systems. In Figs. 10(c) and 10(d), the well width dependence of the total thermal conductivity is displayed for all quantum well systems. It is obtained that κ_{total} values decrease with increasing quantum well width. This is because κ_c has larger values than $\kappa_{bp} + \kappa_{ph}$ thus κ_{total} shows the same trend as in κ_c. At 300 K, the minimum κ_{total} values are found for $d_A = 20$ nm quantum wells as 0.55 W/m K and 1.12 W/m K for 0La and 0.01La quantum well system, respectively.

The temperature variation of thermoelectric figure of merit for both types of quantum well systems is presented in Figs. 11(a) and 11(b) with different quantum well widths. For all quantum wells, ZT increases with temperature owing to their extrinsic semiconductor behavior. Additionally, as seen in Figs. 11(c) and 11(d) for both types of quantum well systems, the thermoelectric figure of merit goes down while the well width increases. This is because for both quantum wells while S and σ improve with reduced d_A, κ_{total} decreases with larger d_A values.

In Fig. 12, to make a clear comparison of thermoelectric transport properties of both bulk and quantum well systems, the temperature dependence of (a) the Seebeck coefficient, (b) the electrical conductivity, (c) the sum of bipolar and

phonon thermal conductivity, and (d) the ZT is represented for all quantum well systems including their bulk solution results. As seen in Fig. 12(d), the $d_A = 10$ nm 0La doped $Mg_2Si/Mg_2Ge/Mg_2Si$ quantum well system has the highest ZT value as 2.41 at 800 K which is because of its highest Seebeck coefficient value and lower $\kappa_{bp} + \kappa_{ph}$ value at that temperature among all quantum well systems. Following that the second highest ZT value is gained as 2.26 for $d_A = 10$ nm 0.01La doped quantum well system whereas it has the highest σ value due to its lowest $\kappa_{bp} + \kappa_{ph}$ value it leads to enhanced ZT value. Compared to the bulk form of $La_xMg_{2-x}Si_{0.49}Sb_{0.01}$ solid solutions (where $x = 0$ and $x = 0.01$), the value of ZT can be improved up to nearly 276% and 133% by using their 0La and 0.01La doped quantum well structures, respectively. From our theoretical calculations, it is found that the Seebeck coefficient is improved significantly with lowering the dimensionality throughout the temperature range for all two types of samples. For the electrical conductivities while for 0La doped samples, σ is reduced by using quantum well forms for 0.01La doped samples; a clear improvement is gained apart from 0.01La doped $d_A = 20$ nm quantum well sample. In addition to these for all samples, a significant reduction is obtained when using the quantum well forms. Thus, these findings suggest that the main source of huge enhancements gained for thermoelectric efficiency actually comes both from the increment in the Seebeck coefficient and the reduction in the phonon thermal conductivity due to the inclusion of additional interface
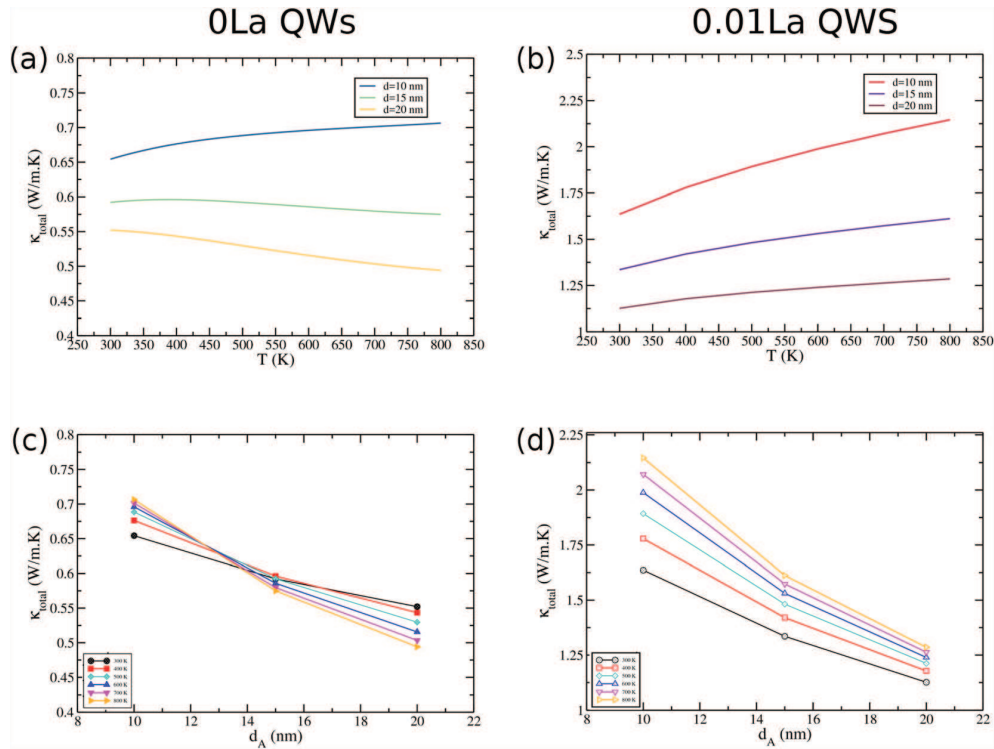
FIG. 10. Temperature dependence of the total thermal conductivity for doped Mg$_2$Si/Mg$_2$Ge/Mg$_2$Si quantum wells with different well widths (chosen as d_A = 10 nm, 15 nm, and 20 nm) (a) for 0La QWs and (b) for 0.01La QWs. The well width dependence of the total thermal conductivity (c) for 0La QWs and (d) for 0.01La QWs.
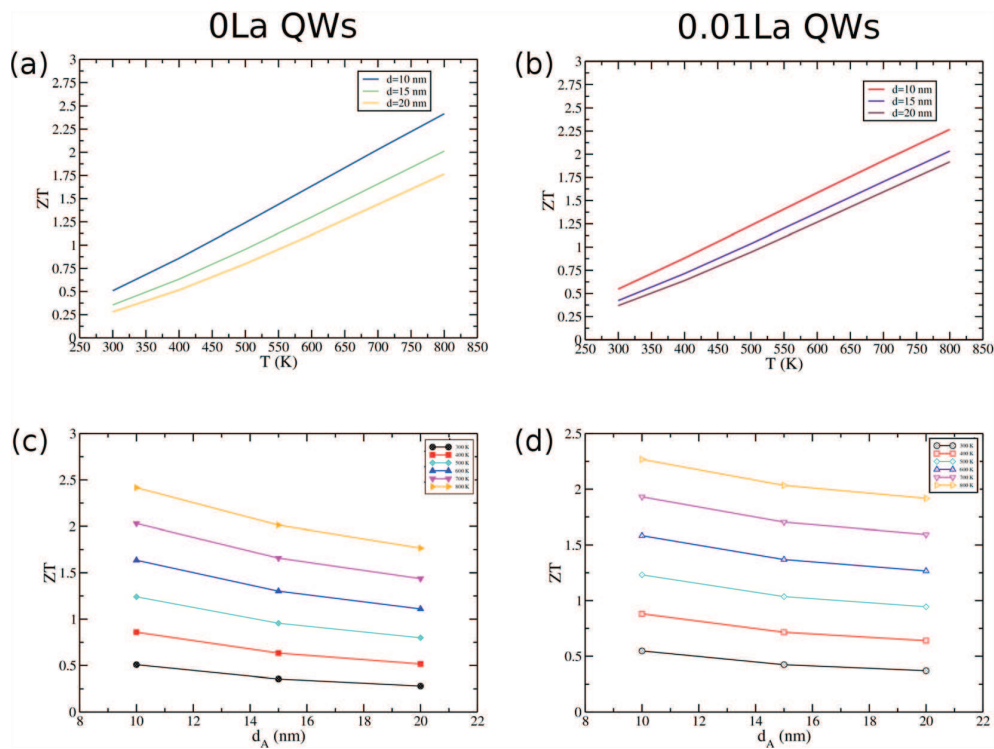

FIG. 11. Temperature dependence of the thermoelectric figure of merit for doped Mg$_2$Si/Mg$_2$Ge/Mg$_2$Si quantum wells with different well widths (chosen as d_A = 10 nm, 15 nm, and 20 nm) (a) for 0La QWs and (b) for 0.01La QWs. The well width dependence of the thermoelectric figure of merit (c) for 0La QWs and (d) for 0.01La QWs.
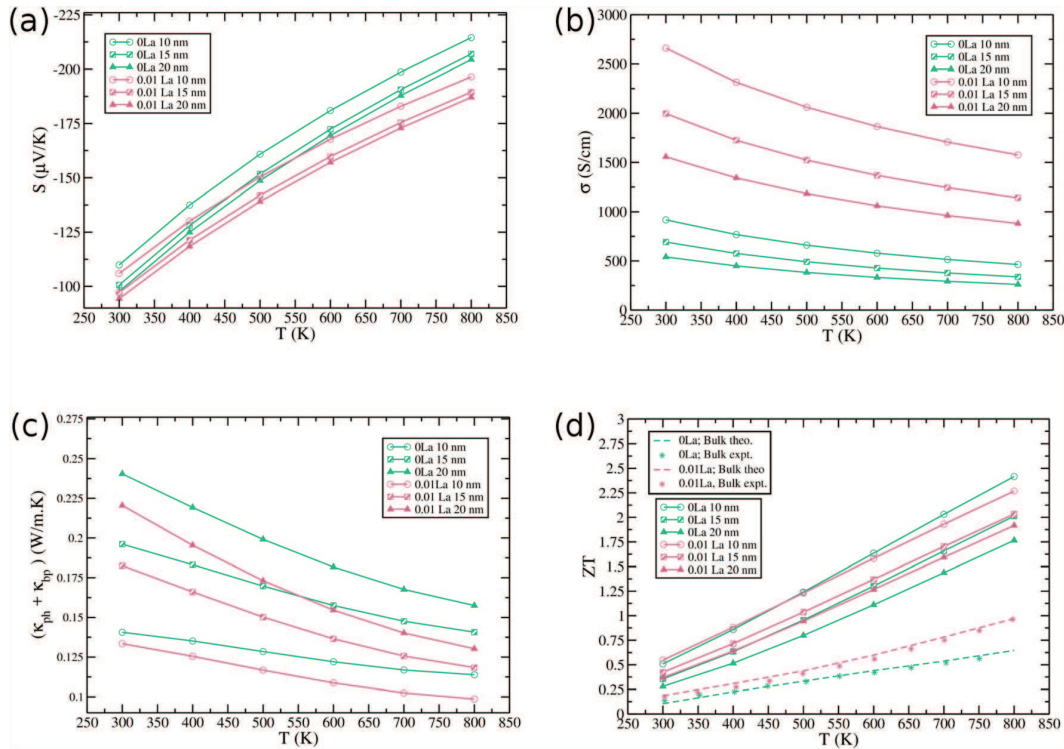
FIG. 12. Comparison of the temperature dependence of (a) the Seebeck coefficient, (b) the electrical conductivity, (c) the sum of phonon and bipolar thermal conductivity and (d) thermoelectric figure of merit of 0La and 0.01La QWs with different quantum well widths chosen as $d_A = 10$ nm, 15 nm, and 20 nm and bulk $La_xMg_{2-x}Si_{0.49}Sb_{0.01}$ solid solutions shown with dashed lines as theoretical results and stars as their experimental measurements, respectively.

mass-mixing and dislocation scatterings, both, with the scaled anharmonic phonon scattering.

IV. CONCLUSIONS

We have presented the results of a theoretical investigation of thermoelectric transport properties of 3D bulk and 2D quantum well systems that establish the proof-of-principle of an enhanced thermoelectric figure of merit at 800 K in thermoelectric quantum wells, presumably as a result of drastically lowered thermal conductivity with the inclusion of additional interface scattering mechanisms, both, with scaled anharmonic phonon scattering. Calculations are performed for n-type doped $La_xMg_{2-x}Si_{0.49}Ge_{0.5}Sb_{0.01}$ solid solutions (where $x = 0$ and $x = 0.01$) and $Mg_2Si/Mg_2Ge/Mg_2Si$ quantum well systems (one of them is only 0.01 wt. % Sb doped, and the other one is doped with both 0.01 wt. % Sb and 0.01 wt. % La). The calculated Seebeck coefficients at 800 K of quantum well systems with 10 nm well widths are about % 6 larger than their bulk forms. While for the 0La doped quantum well systems, larger electrical conductivity values obtained compared to their bulk forms the same trend that is not found for 0.01La doped quantum well systems. For both types of doped 10 nm well width quantum well systems, the minimum values of the sum of bipolar and phonon thermal conductivities at 800 K attained to be 0.11 W/m K and 0.09 W/m K for 0La and 0.01La quantum wells, respectively. Though their bulk forms had he values of 1.53 W/m K and 0.59 W/m K for the samples of with the doping levels as $x = 0$ and $x = 0.01$, respectively. As a result, the 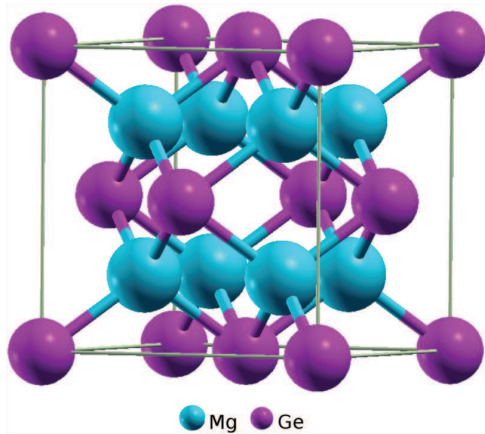best overall ZT at 800 K of quantum well systems are gained for 10 nm well widths as $ZT(0La) = 2.41$ and $ZT(0.01La) = 2.26$ whereas their bulk forms only had the values of $ZT(0La) = 0.64$ and $ZT(0.01) = 0.56$ at the same temperature, respectively. The results of these theoretical calculations show that the quantum well structures can significantly modify and greatly improve the thermoelectric efficiency. The present work suggests that the prospects of using Mg_2X ($X = Si$, Ge) based quantum well structures open the possibility of having new class of mid-temperature thermoelectric materials.

APPENDIX: ELECTRONIC STRUCTURE CALCULATIONS BY USING DENSITY FUNCTIONAL THEORY

Mg_2Ge crystallises in the antiflourite structure (Fig. 13) with a face centered cubic (fcc) Bravais lattice and the space group Fm $\bar{3}$ m. There are three atoms in its primitive

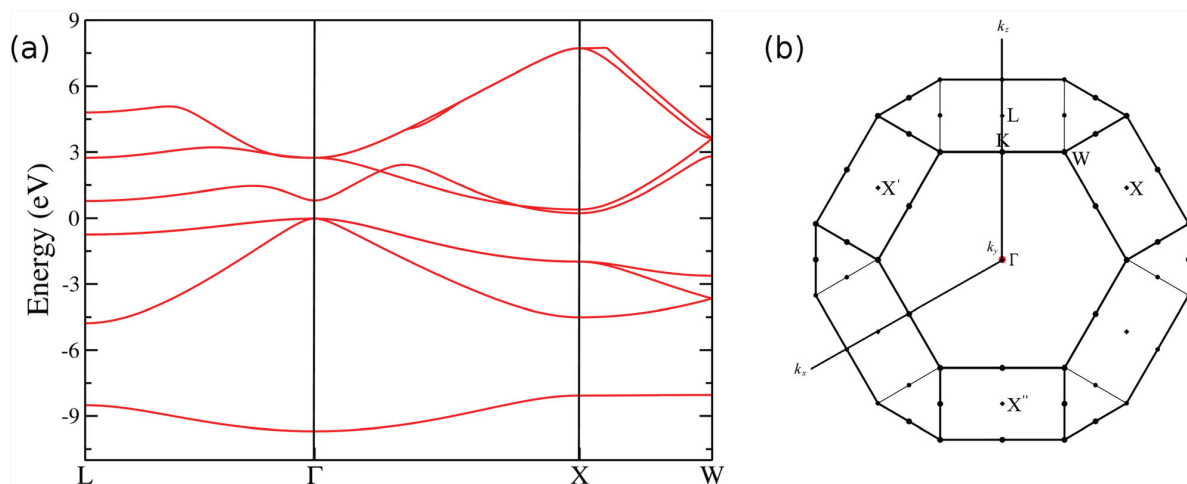FIG. 13. The cubic anti-fluorite-type crystal structure of Mg$_2$Ge.

TABLE III. The calculated lattice constants and band gaps (by applying the functionals of GGA, LDA, and rVV10) of Mg$_2$Ge in comparison with the previous experimental data.

Property	GGA	LDA	rVV10	Experiment
Lattice constant (Å)	6.454	6.314	6.438	6.393[36]
Band gap (eV)	0.20	0.16	0.26	0.74[47]

are allowed to relax until the maximum Hellmann-Feynman force acting on each atom becomes smaller than 0.01 eV Å^{-1}. The convergence criteria for total energy is set to within 10^{-8} Ry.

The calculated lattice constants for Mg$_2$Ge are listed in Table III in comparison with the available experimental data. It is found that from our rVV10 functional result, the lattice constant of 6.438 Å is in a very good agreement with the experimental value of 6.393 Å (Ref. 36) by only 0.7% over-estimation. Additionally, compared to previous computational studies,[45,46] we can conclude that our lattice constant value is much closer to the experimental value. In Fig. 14(a), the band structure of Mg$_2$Ge is plotted, and we found a small indirect band gap value of 0.26 eV where the conduction band minimum is at X point while the valence band maximum is located at the Γ point. The values of calculated band gaps for three different functionals are listed in Table III with its experimental value.[47] We have already known that the DFT functionals generally underestimate the band gaps of semiconductors.

In order to calculate the electron effective mass tensors of Mg$_2$Ge which is strongly required for its thermoelectric transport properties, we evaluate the effective mass tensors by using the formula[48] $m^* = |M|^{1/3}$, where $|M|$ is the determinant of matrix M which represents the effective mass tensors in matrix form. From the dispersion curve of Mg$_2$Ge, it is clearly obtained that for the lowest conduction band, the diagonal effective mass tensors are found to be equal to 0.253m$_e$.

cell where two Mg atoms are located at a(0.25, 0.25, 0.25) and a(0.75, 0.75, 0.75) and one Ge atom is located at a(0, 0, 0) where a is the lattice parameter. The structural and electronic properties of Mg$_2$Ge is investigated in the framework of the density functional theory (DFT) based on the Kohn-Sham equations.[37] The DFT calculations were performed using the plane wave self-consistent field (PWSCF) code as implemented in quantum ESPRESSO.[38] The local density approximation (LDA) described by Perdew-Zunger,[39] generalized the gradient approximation (GGA) described by Perdew-Burke-Ernzerhof (PBE),[40] and van der Waals interaction-corrected density (DFT/rVV10)[41] functionals are used to describe the exchange-correlation of electrons. To describe the interaction between valence electrons and ion cores, we use the ultrasoft pseudopotentials for Mg and Ge atoms in all calculations.[42] The kinetic energy cutoff was set to 60 Ry for the plane wave basis. The integration over the Brillouin zone is performed using a 12 × 12 × 12 Monkhorst-Pack (MP)[43] k-point grid and Methfessel-Paxton[44] smearing of 0.01 Ry. All atoms in the bulk Mg$_2$Ge

FIG. 14. (a) Calculated electronic band structure of Mg$_2$Ge and (b) Brillouin zone for Mg$_2$Ge.

[1] V. K. Zaitsev, M. I. Fedorov, I. S. Eremin, and E. A. Gurieva, *Thermoelectrics Handbook: Macro to Nano Structured Materials* (CRC Press, New York, 2005), Chap. 29.

[2] H. J. Goldsmid, *Thermoelectric Refrigeration* (Plenum, New York, 1964).

[3] B. Poudel, Q. Hao, Y. Ma, Y. Lan, A. Minnich, B. Yu, X. Yan, D. Wang, A. Muto, D. Vashaee, X. Chen, J. Liu, M. S. Dresselhaus, G. Chen, and Z. Ren, Science **320**, 634–638 (2008).

[4] D. Kraemer, B. Poudel, H.-P. Feng, J. C. Caylor, B. Yu, X. Yan, Y. Ma, X. Wang, D. Wang, A. Muto, K. McEnaney, M. Chiesa, Z. Ren, and G. Chen, Nat. Mater. **10**, 532–538 (2011).

[5] G. Mahan, B. C. Sales, and J. Sharp, Phys. Today **50**(3), 42–47 (1997).

[6] P. M. Lee, Phys. Rev **135**, A1110–A1114 (1964).

[7] S. K. Bux, M. T. Yeung, E. S. Toberer, G. J. Snyder, R. B. Kaner, and J.-P. Fleurial, J. Mater. Chem. **21**, 12259–12266 (2011).

[8] V. K. Zaitsev, M. I. Fedorov, E. A. Gurieva, I. S. Eremin, P. P. Konstantinov, A. Y. Samunin, and M. V. Vedernikov, Phys. Rev. B **74**, 045207 (2006).

[9] X. Liu, T. Zhu, H. Wang, L. Hu, H. Xie, G. Jiang, G. J. Snyder, and X. Zhao, Adv. Energy Mater. **3**, 1238–1244 (2013).

[10] W. Liu, Q. Zhang, K. Yin, H. Chi, X. Zhou, X. Tang, and C. Uher, J. Solid State Chem. **203**, 333–339 (2013).

[11] T. Dasgupta, C. Stiewe, R. Hassdorf, A. J. Zhou, L. Boettcher, and E. Mueller, Phys. Rev. B **83**, 235207 (2011).

[12] J.-Y. Jung, K.-H. Park, and I.-H. Kim, Mater. Sci. Eng. **18**, 142006 (2011).

[13] J.-I. Tani and H. Kido, Intermetallics **15**, 1202–1207 (2007).

[14] M. I. Fedorov, V. K. Zaitsev, and G. N. Isachenko, Solid State Phenom. **170**, 286–292 (2011).

[15] A. U. Khan, N. Vlachos, and Th. Kyratsi, Scr. Mater. **69**, 606–609 (2013).

[16] L. D. Hicks and M. S. Dresselhaus, Phys. Rev. B **47**, 12727–12731 (1993).

[17] R. Venkatasubramanian, E. Siivola, T. Colpitts, and B. O'Quinn, Nature **413**, 597–602 (2001).

[18] T. C. Harman, P. J. Taylor, M. P. Walsh, and B. E. LaForge, Science **297**, 2229–2232 (2002).

[19] X. Zhou, G. Wang, H. Chi, X. Su, J. R. Salvador, W. Liu, X. Tang, and C. Uher, J. Electron. Mater. **41**, 1589–1594 (2012).

[20] P. J. Price, Philos. Mag. **46**, 1252–1260 (1955).

[21] G. P. Srivastava, *The Physics of Phonons* (Taylor and Francis Group, New York, 1990).

[22] D. R. Lide, *CRC Handbook of Chemistry and Physics*, 87th ed. (Taylor and Francis Group LLC, 2007).

[23] Ö. C. Yelgel and G. P. Srivastava, Philos. Mag. **94**, 2072–2099 (2014).

[24] Ö. C. Yelgel and G. P. Srivastava, Phys. Rev. B **85**, 125207 (2012).

[25] Ö. C. Yelgel and G. P. Srivastava, J. Appl. Phys. **113**, 073709 (2013).

[26] J. P. McKelvey, *Solid State and Semiconductor Physics* (Harper and Row Publishers, New York, 1966).

[27] R. R. Heikes and R. W. Ure, *Thermoelectricity, Science and Engineering* (Interscience, New York, 1961).

[28] D. M. Rowe and C. M. Bhandari, *Modern Thermoelectrics* (Reston Publishing Company, Virginia, 1983).

[29] T. M. Tritt, *Thermal Conductivity Theory, Properties and Applications* (Kluwer Academic/Plenum Publishers, London, 2004).

[30] M. G. Holland, Phys. Rev. **134**, A471-1–A471-10 (1964).

[31] M. Grundmann, *The Physics of Phonons: An Introduction Including Devices and Nanophysics* (Springer, Berlin, 2006).

[32] O. L. Anderson, J. Phys. Chem. Solids **12**, 41–52 (1959).

[33] S. L. Shinde and J. S. Goela, *High Thermal Conductivity Materials* (Springer, New York, 2006).

[34] J. Mao, Z. Liu, and Z. Ren, NPJ Quantum Mater. **1**, 16028 (2016).

[35] E. I. Rogacheva, S. G. Lyubchenko, and M. S. Dresselhaus, Thin Solid Films **516**, 3411 (2008).

[36] *Non-Tetrahedrally Bonded Elements and Binary Compounds I*, Landolt-Börnstein-Group III Condensed Matter Vol. 41C, edited by O. Madelung, U. Rössler, and M. Schulz (Springer Materials, 1998).

[37] W. Kohn and L. J. Sham, Phys. Rev. **140**, A1133 (1965).

[38] P. Giannozzi, S. Baroni, N. Bonini, M. Calandra, R. Car, C. Cavazzoni, D. Ceresoli, G. L. Chiarotti, M. Cococcioni, I. Dabo, A. Dal Corso, S. Fabris, G. Gougoussis, A. Kokalj, M. Lazzeri, L. Martin-Samos, N. Marzari, F. Mauri, R. Mazzarello, S. Paolini, A. Pasquarello, L. Paulatto, C. Sbraccia, S. Scandolo, G. Sclauzero, A. P. Seitsonen, A. Smogunov, P. Umari, and R. M. Wentzcovitch, J. Phys.: Condens. Matter **21**, 395502 (2009).

[39] J. P. Perdew and A. Zunger, Phys. Rev. B **23**, 5048 (1981).

[40] J. P. Perdew, K. Burke, and M. Ernzerhof, Phys. Rev. Lett. **77**(18), 3865–3868 (1996).

[41] R. Sabatini, T. Gorni, and S. de Gironcoli, Phys. Rev. B **87**, 041108(R) (2013).

[42] D. Vanderbilt, Phys. Rev. B **41**, 7892 (1990).

[43] H. J. Monkhorst and J. D. Pack, Phys. Rev. B **13**(12), 5188–5192 (1976).

[44] M. Methfessel and A. T. Paxton, Phys. Rev. B **40**, 3616–3621 (1989).

[45] J. L. Corkill and M. L. Cohen, Phys. Rev. B **48**, 17138 (1993).

[46] J. Tani and H. Kido, Comput. Mater. Sci. **42**, 531 (2008).

[47] U. Winkler, Helv. Phys. Acta **28**, 633 (1955).

[48] N. W. Ashcroft and N. D. Mermin, in *Solid State Physics*, edited by D. G. Crane (Saunders College Publishing, New York, 1976), Vol. 239.